Progress In Electromagnetics Research C, Vol. 173, 344–356, 2026 PIER C

(Received 22 June 2026, Accepted 13 August 2026, Scheduled 24 September 2026)

Design and System-Level Analysis of a Row-Column Encoded 1-Bit Reconfigurable Metasurface in Payload-Constrained Aerial Platforms

Rifnaldi[1], Rifqi Rizqullah[1], Naufal R. Siregar[1], Suisbiyanto Prasetya[2], Basith A. Asy'ari[1,*], Muhammad Z. Romdlony[1], and Ashif A. Fathnan[1,2,*]

[1]*Department of Electrical Engineering, Telkom University, Bandung, Indonesian*
[2]*Research Center for Telecommunications, National Research and Innovation Agency (BRIN), Bandung, Indonesia*

ABSTRACT: The mitigation of non-line-of-sight (NLoS) blockages in modern multi-user wireless networks increasingly relies on reconfigurable metasurfaces (RMSs) for adaptive beamforming. However, achieving high-resolution phase control typically requires complex, heavy biasing networks, which strictly limit deployment on payload-constrained aerial platforms. To address this, this paper presents the design and system-level performance analysis of a low-profile, 1-bit reconfigurable metasurface operating at 5.67 GHz, developed toward eventual integration on Unmanned Aerial Vehicle (UAV) platforms for real-world NLoS mitigation. Designed on a single-layer dielectric substrate, the 10×10 meta-atom array uses a row-column addressing architecture that drastically reduces control circuitry to just 20 biasing lines, making it a lightweight and readily fabricable candidate for future UAV-mounted deployment. Adaptive twin-beam steering patterns were synthesized across a $\pm 10^\circ$ to $\pm 60^\circ$ design space in which two-tier simulations confirmed reliable beam-pointing accuracy (deviations below 1.5°) for target angles up to $\pm 40^\circ$, while revealing significant pointing degradation at $\pm 50^\circ$ and beyond due to element-pattern roll-off. To assess its potential for payload-constrained applications, the metasurface operation as a UAV-mounted relay was evaluated via a simulated NLoS communication scenario within this validated $\pm 40^\circ$ range. The system shows strong spatial selectivity, effectively isolating targeted users from interference and demonstrating its capability to restore blocked data links under simulated deployment conditions. By delivering a decisive 8 to 14 dB Signal-to-Noise Ratio (SNR) advantage to maintain a stringent 10^{-3} Bit Error Rate (BER), this work establishes the hardware-efficient metasurface as a promising, deployment-ready design for future resilient aerial communication systems, with physical prototyping and real-world flight testing planned as the next stage of this research.

1. INTRODUCTION

The rapid expansion of modern wireless networks, particularly within sub-6 GHz frequency bands, has been driven by the exponential demand for massive connectivity in multi-user environments and emerging Internet of Things (IoT) applications [1, 2]. However, a fundamental challenge in these deployments is the susceptibility of wireless links to severe signal degradation and complete outages caused by physical blockages, such as buildings in dense urban environments [3]. Traditionally, mitigating these non-line-of-sight (NLoS) blind spots required deploying additional active base stations or relays, which significantly increases both infrastructure costs and overall network energy consumption [4]. Recently, Reconfigurable Intelligent Surfaces (RIS), also known as Reconfigurable Metasurfaces (RMSs), have emerged as a promising, energy-efficient paradigm [5–8]. By dynamically altering the electromagnetic properties of their meta-atoms, these surfaces can control the propagation environment, effectively routing signals around obstacles to establish robust communication links [9–11]. Beyond enhancing wireless communication, RMSs are also used for spatial sensing and localization, allowing systems to efficiently scan their environment and pinpoint distant targets [12].

To maximize the spatial flexibility of RMS technology, integrating these surfaces with mobile aerial platforms such as Unmanned Aerial Vehicles (UAVs) has attracted considerable attention [13, 14]. As shown in Figure 1, UAV-mounted metasur-

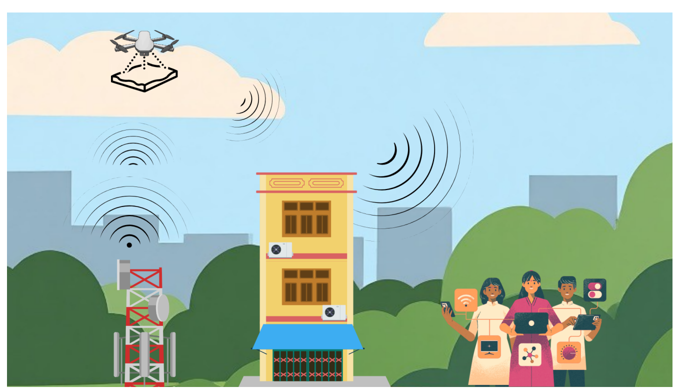

FIGURE 1. Geometric illustration of the proposed UAV-mounted reconfigurable metasurface, dynamically mitigating NLoS blockages to serve distributed terrestrial users.

* Corresponding authors: Basith A. Asy'ari (basithaa@telkomuniversity.ac.id); Ashif Aminulloh Fathnan (ashi001@brin.go.id).

faces can leverage 3D mobility to dynamically position themselves in optimal locations, restoring blocked communication links on demand and serving distributed terrestrial users [15]. Despite this immense potential, the practical deployment of UAV-mounted RMS is strictly bounded by aerodynamic stability and payload limits [16]. Many existing reconfigurable metasurface designs rely on bulky, multi-layer dielectric substrates and complex biasing networks to achieve wideband performance or continuous phase control [17, 18]. Such heavy configurations are severely detrimental to flight time and UAVs' operational efficiency [19]. Consequently, there is a critical need for ultra-lightweight, single-layer metasurface architectures that can maintain high electromagnetic performance without burdening the aerial platform [20].

Among various phase-control techniques, 1-bit coding metasurfaces — typically using PIN diodes to switch between two discrete phase states (e.g., 0° and 180°) — offer an optimal balance among hardware simplicity, low cost, and beamforming efficacy [21–24]. Recent advancements aimed at simplifying the reconfiguration and design of intelligent surfaces have introduced structurally low-complexity unit cells [25] alongside advanced analytical tools such as composite vortex manipulation [26]. However, controlling large-scale arrays remains a significant hurdle. Independent control of every meta-atom in a 2D array dramatically increases the number of control lines, leading to severe routing congestion and increased structural weight [27]. To solve this problem, row-column addressing architectures present a highly hardware-efficient alternative [28–30]. By coupling elements vertically and horizontally, the complexity of the control circuitry is drastically reduced. To translate these 1D row and column constraints into highly functional 2D beamforming patterns, advanced synthesis algorithms, such as the Multiple Partition Cross Modulation (MPCM) encoding scheme, are required [28, 31, 32]. Despite these attempts, translation of these row-column addressing metasurfaces into a design specifically optimized for payload-constrained aerial deployment remains largely unexplored, as prior works require multiple substrate and bonding layers that effectively double the metasurface weight [28]. Moreover, while extensive research has focused on the physical design and full-wave validation of reconfigurable metasurfaces [33, 34], there remains a notable gap in translating these hardware metrics into rigorous, system-level communication performance [35, 36].

To bridge this gap, this paper presents the design, electromagnetic validation, and system-level performance analysis of a 1-bit reconfigurable row-column addressing metasurface operating at 5.67 GHz. The proposed 10×10 array employs a double-metallic-layer structure in which the row and column control paths are realized directly through patch segmentation and a via-connected ground strip. The proposed design requires no additional multi-layer routing or auxiliary biasing layers, ensuring minimal payload weight for aerial platforms. By integrating SMP1340-040LF PIN diodes and employing the row-column addressing scheme, the surface achieves optimized, low-SLL twin-beam steering using only 20 control lines. The primary contributions of this work are twofold: First, a rigorous two-tier electromagnetic validation of the row-coulmn addressing scheme is conducted, comparing analytical Array Factor (AF) modeling with physical full-wave numerical simulations. This analysis demonstrates that the surface maintains high pointing accuracy (deviations $< 1.5^\circ$) up to $\pm 40^\circ$, while explicitly identifying the physical limitations of the row-column architecture at extreme angles ($\geq \pm 50^\circ$). Second, the direct quantification of the surface's communication viability is presented through Monte Carlo-based Quadrature Phase Shift Keying (QPSK) reflectarray simulations. By evaluating spatial selectivity, the system demonstrates an 8 to 14 dB Signal-to-Noise Ratio (SNR) gain for targeted multi-user receivers under dynamic blockage scenarios, thereby establishing a definitive link between hardware-efficient metasurface design and highly reliable aerial wireless network performance.

2. RECONFIGURABLE METASURFACE DESIGN AND UNIT CELL SIMULATION

2.1. Row-Column Encoded Reconfigurable Metasurface Design

The practical deployment of UAV-mounted Reconfigurable Metasurfaces (RMSs) is strictly bounded by payload capacities and aerodynamic stability, necessitating ultra-lightweight hardware designs. Traditional metasurfaces that feature fully independent element control require a dedicated biasing line for every meta-atom. For a 10×10 array, this translates to 100 individual control lines, which inevitably leads to severe routing congestion, requires bulky multi-layer printed circuit boards (PCBs), and significantly increases the device's structural weight. To overcome this limitation, the proposed design implements a cross-wired "mesh matrix" configuration, widely recognized in array synthesis as a row-column (RC) addressing architecture. By coupling elements vertically and horizontally, the entire array can be controlled using only 20 biasing lines (10 rows and 10 columns). This dramatic reduction in hardware complexity allows the RMS to be fabricated on a single, ultra-lightweight substrate layer, making it highly suitable for UAV integration.

The fundamental building block of this mesh matrix configuration is a square-shaped meta-atom with dimensions of $25\,\text{mm} \times 25\,\text{mm}$ ($L \times W$), designed to operate in the sub-wavelength regime at 5.67 GHz ($\lambda \approx 52.9\,\text{mm}$). As depicted in Figures 2(a) and (b), the meta-atom structure consists of three layers: a segmented copper patch on the front, a 0.813 mm-thick Rogers RO4003C dielectric substrate in the center, and a ground plane on the back. To facilitate the row-column biasing, the top patch is divided into distinct vertical segments separated by gaps (denoted by the parameter $L8$, with the main center gap being 1 mm wide). Table 1 summarizes the meta-atom's dimensional details.

The left segment of the top patch forms a continuous vertical line across the array, acting as the column control (see Figure 2(c)). In contrast, the right segment is isolated on the top layer but is connected through a via hole to a continuous horizontal metal strip etched into the ground plane on the back, acting as the row control. This bottom metal layer simultaneously serves as the continuous ground plane required to make the structure a fully reflective metasurface (see Figure 2(d)). An SMP1340-040LF PIN diode is mounted across the 1 mm

TABLE 1. Design parameters for the meta-atom metasurface antenna.

Parameters	Value (mm)	Parameters	Value (mm)
L	25	$W3$	0.5
$L1$	9.5	$W4$	9
$L2$	13.5	$W5$	25
$L3$	2	$W6$	9
$L4$	1	$D1$	1
$L5$	0.6	G	0.5
$L6$	11.4	$G1$	15.55
$L7$	11.4	$G2$	9.55
$L8$	1	$G3$	11.5
W	25	$G4$	11.5
$W1$	23	WA	250
$W2$	1	LA	250

center gap, bridging the segments. By applying a positive DC bias voltage to a specific vertical patch on the top layer and grounding the corresponding horizontal segment on the bottom layer, the diode at that exact intersection is forward-biased. This mechanism allows the array to toggle between horizontal and vertical configurations, altering the surface current distribution and phase response without complex multi-layer routing. Note that the incident electric field is polarized in the x-direction as shown in Figure 2. Additionally, note that unintended activation at non-targeted row-column intersections is inherently prevented by the array's physical structure. Adjacent row-to-row and column-to-column segments are separated by small physical gaps, providing direct galvanic isolation between non-intersecting control lines, while row control lines (embedded in the ground plane) and column control lines (on the top patch layer) are further isolated from one another by a 0.813 mm-thick Rogers RO4003C dielectric substrate. Consequently, a given PIN diode is forward-biased only when its corresponding column line is held at a positive DC voltage, and its corresponding row line is simultaneously grounded; diodes at any other row-column combination remain reverse-biased, since they do not receive this specific voltage-and-ground pairing.

To accurately account for conductor losses in the simulation, the patch and ground plane use annealed copper, modeled as a lossy metal with an electrical conductivity of $\sigma = 5.8 \times 10^7$ S/m. The Rogers RO4003C dielectric substrate was selected for its excellent high-frequency stability, featuring a relative dielectric constant (ε_r) of 3.55, relative permeability of 1, and loss tangent ($\tan\delta$) of 0.0027. The PIN diode is modeled as a series RLC circuit. Under forward bias (ON state), the diode is represented by a resistance of $1\,\Omega$, an inductance of 0.45 nH, and a capacitance of 0 pF. In the reverse-biased (OFF state), the resistance increases to $10\ \Omega$ and the capacitance to 0.16 pF, while the inductance remains at 0.45 nH. These parameters are derived directly from the component datasheet. The impedance difference between these two equivalent circuits provides the reflection phase contrast, which is subsequently used to form 1-bit phase encoding on the metasurface array.

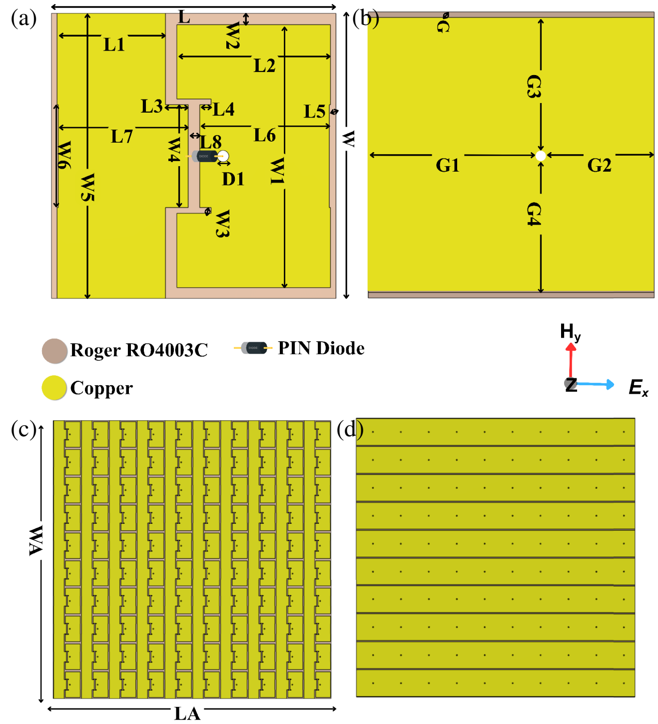

FIGURE 2. Design and geometrical parameters of the reconfigurable metasurface: (a) unit cell structure, front view, (b) rear view, (c) full structure 10×10 array, front view, and (d) rear view.

To substantiate the suitability of the proposed design for payload-constrained aerial deployment, an approximate component-level mass budget was evaluated. The core metasurface structure totals approximately 140 g, which comprises a 250 mm $\times$ 250 mm Rogers RO4003C substrate ($\approx$ 91 g, based on a material density of 1.79 g/cm^3), a segmented copper patch, ground-plane layers ($\approx$ 39 g combined, assuming standard 1 oz copper cladding), 100 SMP1340-040LF PIN diodes ($\approx$ 0.7 g), and row-column biasing wiring ($\approx$ 10 g). The requisite control electronics — consisting of a microcontroller, 20-channel driver circuitry for the biasing lines, a control PCB, and connecting cables — add an estimated 40 g. Furthermore, a rigid mounting bracket to secure the assembly to the UAV frame is estimated at 87 g, assuming a lightweight, ribbed 3D-printed PLA structure. This yields a total component-level mass of approximately 267 g. Even when incorporating conservative engineering margins for protective housing, auxiliary connectors, and fabrication tolerances, the final payload mass remains well below 1 kg. This confirms the system's strict compatibility with the payload capacities of small quadcopter UAVs commonly used for aerial metasurface deployments.

2.2. Simulated Unit-Cell Characteristics

The unit cell was characterized via full-wave simulations in Computer Simulation Technology (CST) Microwave Studio Suite by applying "unit cell" periodic boundary conditions to the x and y axes, and an open boundary was applied on the z-axis, coupled with a Floquet port serving as the wave-stimulus source.

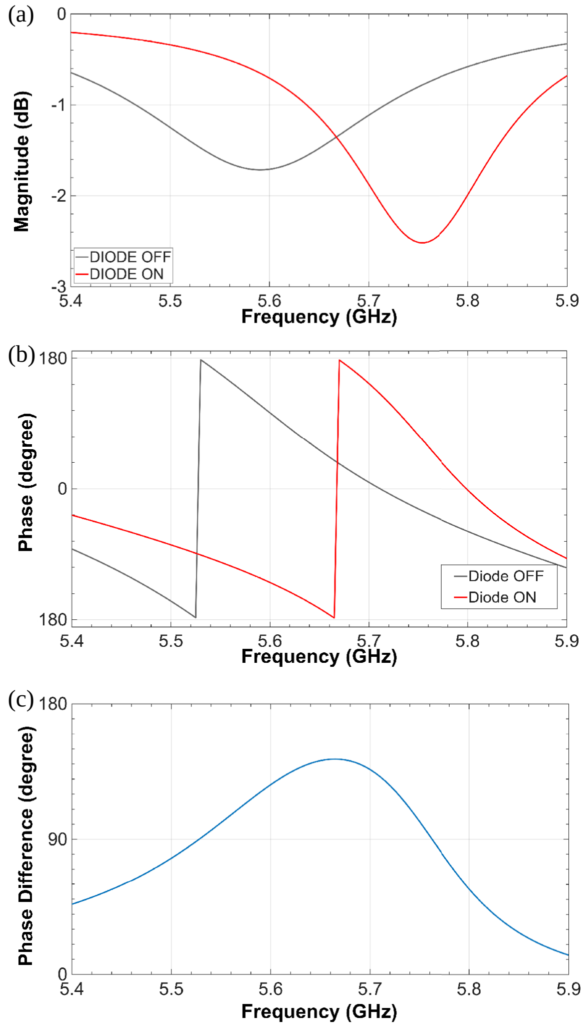

FIGURE 3. Unit cell simulation results: (a) reflection magnitude, (b) reflection phase, and (c) phase difference between ON and OFF states.

Figure 3(a) plots the reflection amplitude for both diode states. The reflection magnitude remains above -2.6 dB across the entire observed spectrum, confirming that most incident wave energy is reflected, and absorption losses are minimal, which are mandatory conditions for an efficient reflective metasurface. The curves display resonance valleys corresponding to phase shifts. The OFF state reaches a minimum reflection magnitude of approximately -1.72 dB at 5.59 GHz, while the ON state reaches -2.50 dB at 5.76 GHz. At the target operating frequency of 5.67 GHz, the reflection magnitudes are nearly identical at -1.33 dB (OFF) and -1.39 dB (ON), corresponding to linear amplitudes of 0.858 and 0.852, respectively. Figure 3(b) shows the reflection's phase response as a function of frequency for both diode conditions. Both curves show distinct resonance positions where the OFF condition curve (black) transitions at approximately 5.53 GHz, whereas the ON condition curve (red) shifts to a higher frequency around 5.67 GHz. This resonance shift is the fundamental mechanism driving the phase difference required for beamforming.

Figure 3(c) plots the resulting phase difference between ON and OFF states as a function of frequency. The phase difference peaks precisely at 5.67 GHz. At this target frequency, the OFF condition yields a reflection phase of $34.40°$, while the ON condition shifts to $177.55°$, producing a maximum phase difference of $143.15°$. Because this frequency provides optimal phase contrast for 1-bit spatial encoding, 5.67 GHz was established as the operating frequency for the array. Table 2 summarizes final extracted excitation parameters.

TABLE 2. Parameters for diode condition at 5.67 GHz.

Diode State	Binary State (s_n)	Amplitude (a_n)	Phase (ϕ_n)
OFF	0	0.858	$34.40°$
ON	1	0.852	$177.55°$

3. ARRAY CONFIGURATION AND SIMULATION RESULTS OF FULL 10×10 RMS STRUCTURE

3.1. Row-Column Configuration and State Mapping

The metasurface array consists of a 10×10 grid of meta-atoms arranged in the x and y planes with a uniform inter-element spacing of $d = 25$ mm along both axes. Each meta-atom in the array can be in one of two diode states, represented by the binary state variable $s_n \in \{0, 1\}$, where $s_n = 0$ for the OFF state and $s_n = 1$ for the ON state. Based on S-parameters extracted in Table 2, the excitation amplitude and phase of each element can be mapped from these binary states via:

$$a_n = a_{\mathrm{OFF}} + (a_{\mathrm{ON}} - a_{\mathrm{OFF}})s_n \quad (1)$$

$$\phi_n = \phi_{\mathrm{OFF}} + (\phi_{\mathrm{ON}} - \phi_{\mathrm{OFF}})s_n \quad (2)$$

with $a_{\mathrm{OFF}} = 0.858$, $\phi_{\mathrm{OFF}} = 34.40°$, $a_{\mathrm{ON}} = 0.852$, and $\phi_{\mathrm{ON}} = 177.55°$. This linear mapping provides two possible excitation conditions for each element, which forms the basis of 1-bit phase encoding in the metasurface array.

The pattern encoding on this metasurface is achieved by applying independent control voltages to row (x) and column (y) lines. Because the row and column biasing networks operate independently, applying a voltage to row x or column y activates all meta-atoms along that respective row or column. Consequently, the resulting 2D pattern is formed by the direct spatial superposition of activated 1D rows and columns. In the realization, the metasurface employs static DC biasing, where all selected control lines are held at a constant voltage simultaneously, allowing the active meta-atoms to continuously sustain their targeted reflection phases. While a fully independent 10×10 array would offer 2^{100} possible phase configurations, the proposed row-column mesh architecture intrinsically couples states of the meta-atoms. Because the 2D phase distribution is dictated by the intersection of 1D rows and 1D columns, the resulting phase pattern evaluated in this simulation is mathematically separable. For a 10-element linear sequence, there are $2^{10} = 1024$ possible state configurations. By computing 1D responses, this study directly synthesizes 1D beamforming patterns. While the current simulation restricts its scope to these separable 1D profiles, this structural framework is inherently compatible with dynamic space-time coding algorithms. In future hardware implementations, advanced schemes, such as Multiple Partition Cross Modulation (MPCM) [28], can be applied directly to this architecture to break the separable limitation and efficiently synthesize fully functional, non-separable 2D spatial profiles.

To evaluate these states, the far-field radiation pattern is calculated using the Array Factor (AF) equation. For an array with inter-element spacing d and excitation of the n-th element expressed as a pair of amplitude a_n and phase ϕ_n, the AF as a function of the angle relative to the main lobe direction is given by [37, 38]:

$$\mathrm{AF}(\theta)=\sum_{n=1}^{N} a_n \exp\left(j\left[kd\left(n-\frac{N+1}{2}\right)\sin\theta+\phi_n\right]\right), \quad (3)$$

where $N = 10$ denotes the number of elements; $k = 2\pi/\lambda$ is the wavenumber; and λ is the wavelength at the operating frequency. The term $(n-\frac{N+1}{2})$ in Equation (3) places the phase reference point at the center of the array, so that the resulting pattern is symmetric about the main lobe direction ($\theta = 0°$) when all elements are in phase. The resulting patterns are then normalized relative to their peak values to facilitate analysis and comparison across configurations:

$$\mathrm{AF}_{\text{norm}}(\theta) = \frac{\mathrm{AF}(\theta)}{\max|\mathrm{AF}(\theta)|} \quad (4)$$

The beam direction θ_{beam} can be determined from the angular position that yields the value $\mathrm{AF}_{\text{norm}}(\theta) = 1$:

$$\theta_{\text{beam}} = \arg\max_{\theta}(\mathrm{AF}(\theta)) \quad (5)$$

3.2. Beamforming Optimization and Simulation Strategy

Because the row-column architecture relies on separable 1D gradients, it cannot perfectly recreate arbitrary 2D phase gradients. This mathematical constraint inherently introduces quantization errors, which typically appear as elevated side-lobe levels (SLLs). Therefore, an optimization strategy is required to find the "best fit" configuration that minimizes energy leakage.

All 1,024 configurations are comprehensively evaluated using a MATLAB analytical script based on the AF formulation. SLL is a key metric for evaluating radiation pattern quality, representing the ratio of the highest sidelobe amplitude to the main lobe:

$$\mathrm{SLL}_{\text{dB}} = 20\log_{10}\left(\frac{|\mathrm{AF}_{\text{sidelobe\_max}}|}{|\mathrm{AF}_{\text{main\_lobe}}|}\right). \quad (6)$$

where $|\mathrm{AF}_{\text{sidelobe\_max}}|$ denotes the peak amplitude of the highest sidelobe outside the main lobe region. The targeted pattern is a twin-beam, featuring two symmetrical main lobes at $+\theta$ and $-\theta$. Therefore, the definition of SLL is adapted to the highest peak outside these two main lobes [6]. The algorithm sorts all local peaks from highest to lowest, selecting the third peak as the SLL value. A lower SLL value indicates a superior beam-steering quality, concentrating radiation energy into targeted multi-user directions while mitigating unwanted interference.

To ensure the highest degree of rigor, a complementary two-tier validation strategy was employed using both MATLAB and CST Microwave Studio:

- **Tier 1: Analytical Optimization (MATLAB):** The AF calculation in MATLAB computes in milliseconds, making it highly effective for rapid algorithmic sorting (the Multiple Partition Cross Modulation or MPCM method) to find optimal states among thousands of possibilities. However, the AF approach assumes isotropic radiators and fundamentally ignores mutual coupling between adjacent unit cells and element pattern roll-off at wide angles.
- **Tier 2: Full-Wave Physical Validation (CST):** Due to the extreme computational cost of solving a full 10×10 mesh matrix with discrete lumped diode elements, CST cannot be used to optimize states. Instead, it is used to validate the physical reality of the specific configurations selected by MATLAB. Specifically, full-wave simulation is performed at the individual unit-cell level to extract the true $\cos^q(\theta)$ element pattern and complex reflection coefficients of the physical structure. The full 10×10 far-field radiation pattern is then synthesized using CST's inherent Array Factor calculation. Because this approach maps the isolated unit-cell response onto a spatial grid rather than solving the entire finite array electromagnetically, dynamic mutual coupling between dissimilar adjacent states (e.g., ON next to OFF) and finite edge effects are not explicitly captured.)

For the +10° configuration, MATLAB calculates the main-lobe direction at 7.30°, while CST provides a value of 7.00°. Each element in the CST 3D model was configured according to the amplitude and phase pairs mapped from the binary states calculated in MATLAB. The far-field results of the CST simulation were then directly compared with analytical patterns to evaluate the metasurface's true physical performance.

3.3. Full Structure Simulation Results

For each state configuration $s = [s_1, s_2, \ldots, s_{10}]$, the array factor $\mathrm{AF}(\theta)$ is calculated using Equation (3), then normalized as shown in Equation (4). From the normalized pattern, two characteristic quantities are extracted: the direction of the main beam θ_{beam} using Equation (5), and the SLL values using Equations (6) and (7) with a twin-beam adaptation. The result of this process is a comprehensive database containing 1,024 pairs, which serves as a reference for the selection stage. For selecting reflection angles, twelve targets were used for evaluation, namely $\pm10°$, $\pm20°$, $\pm30°$, $\pm40°$, $\pm50°$, and $\pm60°$. This selection is intended to verify the twin-beam characteristics of the resulting radiation pattern and evaluate beam-steering performance at the two reflection angles.

The selection was implemented in MATLAB, with the angular resolution for the AF calculation set to $N_0 = 1000$ points evenly distributed across the angular range from $-90°$ to $+90°$. Peak detection was performed using the `findpeaks` function, and the SLL was calculated as the third-highest peak because the twin-beam criterion was used. Table 3 summarizes pattern selection results for all twelve angles, along with the binary state, actual direction produced, and SLL values in dB and linear scales calculated using MATLAB. The results in this table show that the proposed metasurface can direct reflections with

TABLE 3. Pattern selection results from MATLAB.

Degree (°)	Binary State (s_n)	Main Lobe (°)	SLL (dB)
10	1111100000	7.30	−10.41
20	1100011110	18.83	−5.28
30	1001100010	31.44	−3.29
40	0110010010	42.25	−4.10
50	1101001011	50.90	−3.34
60	0101101000	61.89	−1.73
−10	1100000011	−12.52	−3.12
−20	0111100011	−18.83	−5.28
−30	1100110011	−30.54	−5.39
−40	1011001101	−39.55	−3.53
−50	1100101101	−47.48	−4.00
−60	0001011010	−61.89	−1.73

a small beam-direction deviation toward the target, generally less than 3° across the entire steering range ±60°.

To validate results of MATLAB array factor calculations, each of the twelve selected configurations was resimulated in CST Microwave Studio using an array model with a 10×10 matrix configuration. Each element in CST was configured according to the amplitude and phase pairs mapped from the binary state of the selection results in Table 3. Far-field results of the CST simulation were then compared with patterns calculated by MATLAB. Figure 4 shows a far-field comparison in polar coordinates normalized to a linear scale of 0 and 1 between the array factor calculations in MATLAB (blue curve) and the simulations in CST Microwave Studio (red curve) for the twelve patterns, each accompanied by a visualization of a 10×10 matrix. The green cells represent elements in the ON state ($s_n = 1$), while the red cells represent the OFF state ($s_n = 0$).

For configuration at the target angle ±10°, the far-field comparison shows excellent agreement between the MATLAB results and the CST simulation. All the resulting radiation patterns show a twin-beam characteristic with two symmetrical main lobes at angles of $+\theta$ and $-\theta$ perpendicular to the array's normal direction. For the +10° configuration, MATLAB calculates the main lobe direction at 7.30°, while CST provides a value of 7.00°. Similarly, for the −10° configuration, MATLAB returns −12.52° and CST returns −12.00°.

Next, for ±20°, ±30°, and ±40° configurations, the difference in angular values between MATLAB calculations and CST simulations ranges from 1° to 1.25°. This difference remains within an acceptable tolerance for beam-steering applications and indicates that the metasurface can still maintain steering accuracy at intermediate angles. At the −50° configuration, results from MATLAB and CST continue to show consistent agreement with beam directions of −47.48° and −46.00°, respectively, representing a deviation of 1.48°. However, at the +50° configuration, a significant discrepancy arises. MATLAB calculates the main lobe direction at 50.90°, while CST identifies the peak at 14.00°. This 36.90° difference indicates that at certain configurations within the extreme angle range, there is a shift in radiation-pattern characteristics that cannot be fully represented by the array factor model in MATLAB. A similar condition is also observed in the ±60° configuration. MATLAB calculates the beam direction at 61.89° and −61.89° for +60° and −60° configurations with states 0101101000 and 0001011010, and CST provides angles of 3.00° and −3.00°.

The significant difference at angles approaching the ±90° limit indicates that the radiation pattern from MATLAB with a uniform radiation distribution across all angles no longer accurately represents the physical array response calculated from CST. In the CST simulation, the total radiation pattern is the product of the array factor and the element pattern of the meta-atom, where the element pattern experiences a significant reduction at angles above ±50° from the normal direction. The discrepancy is primarily attributed to the element-pattern roll-off at wide angles, which is inherently captured in the CST simulation via the full physical array geometry but is entirely absent from the isotropic-radiator assumption underlying the MATLAB Array Factor formulation. This effect becomes more pronounced at extreme beam angles approaching ±90°, where the element pattern contribution deviates most significantly from an isotropic response, particularly for configurations with complex, highly alternating ON/OFF state distributions.

Results in Table 4 show that the difference between these two values varies depending on the beam-steering configuration. For configurations ranging from ±10° to ±30°, the SLL from the CST simulation tends to be lower than that from MATLAB. For example, at the +10° configuration, MATLAB yields an SLL of −10.41 dB while CST yields −24.88 dB, and at the −10° configuration, values are −3.12 dB in MATLAB and −8.55 dB in CST. The sidelobe angle locations within this range are also consistent between the two methods, with deviations generally under 1°. Conversely, at +40°, ±50°, and ±60° configurations, the SLL from numerical simulation (CST) is actually higher than the AF calculation. For example, at +50°, the AF SLL is −3.34 dB while CST's is only −0.15 dB, indicating a sidelobe whose amplitude is nearly equivalent to the main lobe. This applies not only to the SLL magnitude but also to the sidelobe's angular location. In the +50° configuration, MATLAB identifies a sidelobe at −14.32°, while CST identifies it at −49.00°; similarly, at +60°, it is at 3.33° in MATLAB and at −53.00° in CST, and a similar pattern is observed at −60°. This large shift in angular location indicates that, at angles approaching ±90°, taken together, these results indicate that the degradation at extreme steering angles arises from a combination of these mechanisms, with element-pattern roll-off as the primary driver, and finite-array effects, phase quantization, and mutual coupling acting as secondary contributors. The structure of the radiation pattern undergoes changes that cannot be captured by the analytical array factor formulation.

At +10°, despite a small ΔMain of only 0.30°, the ΔSLL reaches +14.47 dB, indicating that even at well-validated steering angles, the analytically predicted sidelobe level can differ substantially from the full-wave result. More critically, at the extreme angles of +50°, +60°, and −60°, the ΔMain values reach 36.90°, 58.89°, and 58.89°, respectively — deviations on the order of tens of degrees rather than fractions of a de-

TABLE 4. Comparison of far-field radiation metrics between MATLAB and CST simulations.

	MATLAB			CST			Difference	
Target (°)	Main (°)	Side (°)	SLL (dB)	Main (°)	Side (°)	SLL (dB)	ΔMain (°)	ΔSLL (dB)
+10	7.30	37.03	−10.41	7.00	36.00	−24.88	0.30	+14.47
+20	18.83	−0.09	−5.28	18.00	0.00	−9.40	0.83	+4.12
+30	31.44	2.97	−3.29	31.00	3.00	−3.62	0.44	+0.33
+40	42.25	1.89	−4.10	41.00	2.00	−2.90	1.25	−1.20
+50	50.90	−14.32	−3.34	14.00	−49.00	−0.15	36.90	−3.19
+60	61.89	3.33	−1.73	3.00	−53.00	−6.28	58.89	+4.55
−10	−12.52	−31.08	−3.12	−12.00	−31.00	−8.55	0.52	+5.43
−20	−18.83	0.09	−5.28	−18.00	0.00	−9.40	0.83	+4.12
−30	−30.54	−0.09	−5.39	−30.00	0.00	−7.88	0.54	+2.49
−40	−39.55	68.56	−3.53	−39.00	0.00	−3.39	0.55	−0.14
−50	−47.48	−0.09	−4.00	−46.00	0.00	−1.18	1.48	−2.82
−60	−61.89	−3.33	−1.73	−3.00	53.00	−6.33	58.89	+4.60

gree, confirming that beyond $\pm 40°$, the array factor model no longer provides a physically reliable prediction of the beam direction. These substantial shifts are concentrated specifically at target angles $\geq \pm 50°$, reinforcing the $\pm 40°$ practical operating limit identified in Section 3.3. The right two columns in Table 4 show the difference between the MATLAB calculations and the CST simulations for the main lobe (ΔMain) and side lobe level (ΔSLL).

It is worth noting that the obtained phase contrast of 143.15° deviates from the ideal 180° condition typically targeted for 1-bit phase encoding, corresponding to a phase error of 36.85°. To quantify the impact of this deviation on beamforming performance, a benchmark comparison was performed between the actual diode-based excitation ($a_{\mathrm{OFF}} = 0.858\angle 34.40°, a_{\mathrm{ON}} = 0.852\angle 177.55°$) and an idealized 1-bit condition (unity reflection amplitude, exact 180° phase contrast), applied to identical binary state configurations across all twelve target angles evaluated in Table 3. With respect to beam-pointing accuracy, the results as shown in Figure 4 indicate that the average beam-direction deviation from the target angle is comparable between the two conditions (approximately 1.3° for the ideal case versus 1.6° for the actual case), with both remaining below 2.7° across the full $\pm 10°$ to $\pm 60°$ design range. This shows that the main beam direction is governed primarily by the inter-element phase progression dictated by the selected binary state pattern rather than by the magnitude of the phase contrast itself, confirming that the non-ideal phase contrast does not substantially compromise steering accuracy. The effect of the non-ideal phase contrast is instead concentrated in the sidelobe level. The ideal 180° condition achieves a lower (more negative) third-peak SLL than the actual 143.15° configuration in eleven of the twelve evaluated angles, with an average SLL improvement of approximately 1.1 dB and a maximum improvement of 4.25 dB observed at $-30°$; only at $+10°$ does the actual configuration show a marginally lower SLL, attributed to a small shift in secondary-peak location rather than a systematic advantage. This confirms that the residual sidelobe level observed in our design results from imperfect destructive cancellation between ON and OFF elements caused by the phase deviation from the ideal condition. Since the physical array geometry, element spacing, and boundary conditions remain identical between actual and ideal cases — only the per-element excitation amplitude and phase differ — this SLL degradation is attributed specifically to non-ideal phase contrast rather than to mutual coupling, whose contribution should remain effectively unchanged between the two cases given the fixed array geometry. While further optimization of the unit-cell geometry could yield a phase contrast closer to the ideal 180°, such component-level refinements fall outside the scope of this work.

4. SYSTEM-LEVEL COMMUNICATION PERFORMANCE

4.1. Wireless Communication Setup and Simulation Scenario

While previous sections validated the electromagnetic performance of the row-column encoded metasurface — demonstrating accurate beam pointing and low Side-Lobe Levels (SLLs) up to $\pm 40°$ — these physical-layer hardware metrics do not inherently quantify data transmission reliability. For practical deployment, particularly when the RMS is mounted on a UAV to restore communication links blocked by urban infrastructure, it is critical to translate these radiation patterns into system-level communication performance. To bridge this gap, this section evaluates spatial selectivity and signal robustness using standard modulation schemes, to evaluate the physical beam-steering accuracy towards reliable multi-user data links.

To evaluate this system-level performance, a simulation scenario was designed to emulate a typical NLoS (Non-Line-of-Sight) wireless communication environment aided by a UAV-mounted RMS. As depicted in Figure 5, the scenario consists of a ground transmitter placed directly below the metasurface at coordinates $(0, 0)$, a metasurface antenna hovering at a height of $H = 10$ m at coordinates $(0, H)$, and three spatially distributed ground receivers (Rx1, Rx2, Rx3) positioned at angles of $+20°$, $+30°$, and $+40°$ relative to the normal direction of the metasurface. The transmitter emits a vertically modulated sig-

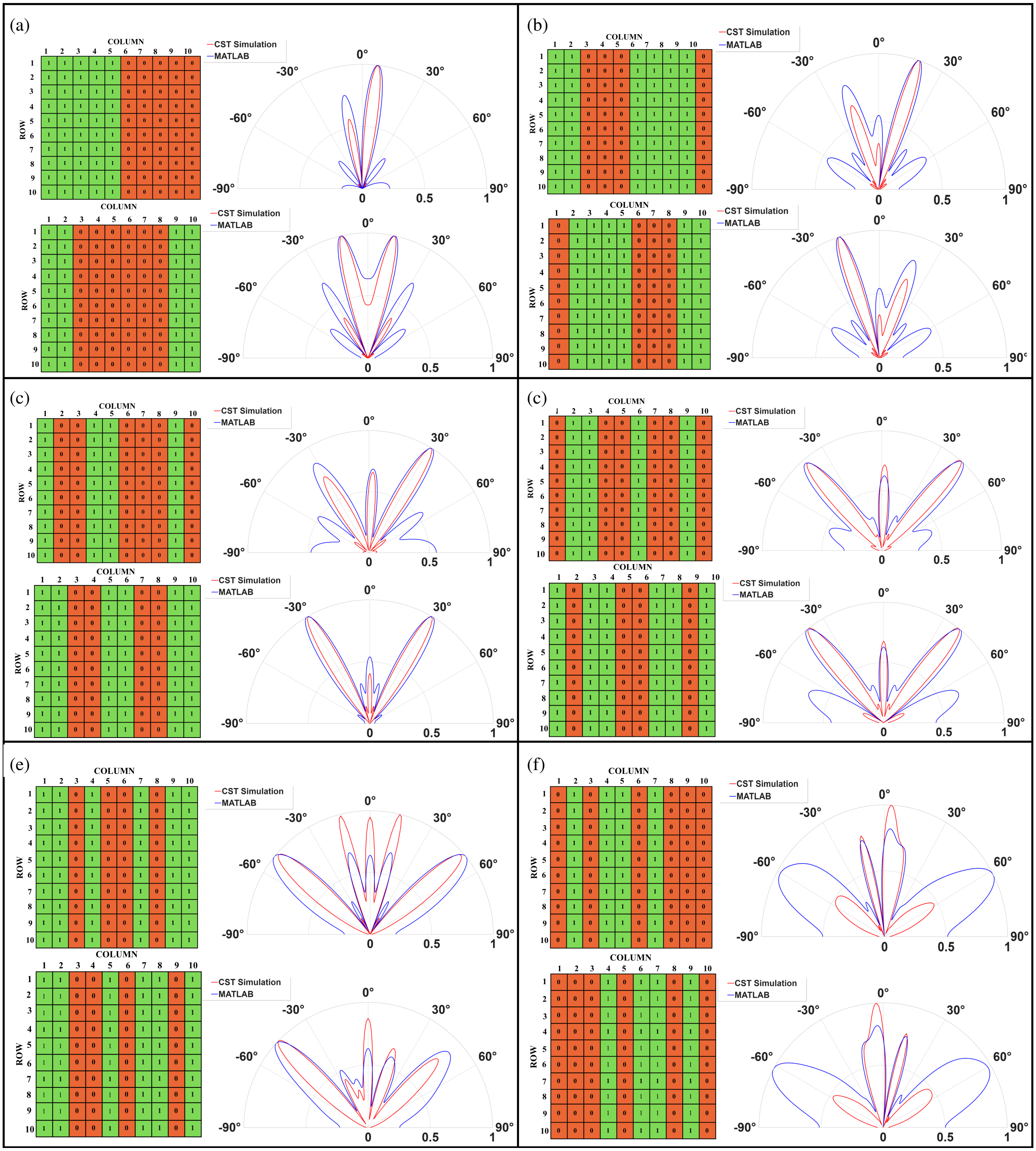

FIGURE 4. Normalized far-field radiation patterns comparing the simulation using MATLAB and CST for target steering angles of (a) $\pm 10^\circ$, (b) $\pm 20^\circ$, (c) $\pm 30^\circ$, (d) $\pm 40^\circ$, (e) $\pm 50^\circ$, and (f) $\pm 60^\circ$.

nal upward, resulting in a perpendicular angle of incidence on the metasurface. The RMS then redirects the signal toward the targeted receivers according to the activated 1-bit phase pattern. The horizontal position (X_r) and slant distance (r_r) of each receiver are calculated using trigonometry based on right-angled triangles formed between the UAV height and the ground projection:

$$X_r = H \tan \theta_r, \tag{7}$$

$$r_r = \frac{H}{\cos \theta_r}. \tag{8}$$

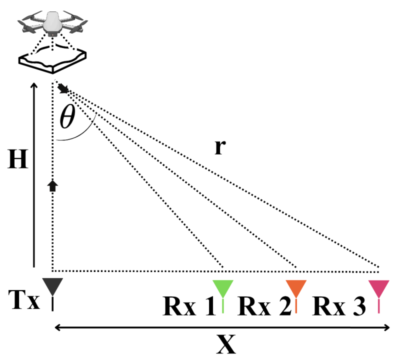

FIGURE 5. Geometric model of the communication scenario, illustrating the spatial relationship between the ground transmitter, the UAV-mounted metasurface, and the distributed receivers.

Here, X_r is the horizontal distance from the origin to the receiver, and r_r is the actual path length traveled by the reflected electromagnetic wave. Table 5 summerizes resulting spatial coordinates for the three receivers.

TABLE 5. Position of the three ground receivers.

Receiver	Angle θ (°)	X (m)	r (m)
Rx1	+20	3.64	10.64
Rx2	+30	5.77	11.55
Rx3	+40	8.39	13.05

4.2. Channel Modeling and Modulation Scheme

The evaluated architecture adopts a Reconfigurable Intelligent Surface (RIS) paradigm [5, 6]. Signal modulation is performed entirely at the active ground transmitter. The UAV-mounted metasurface acts as a passive, reconfigurable reflector, using the 1-bit phase encoding on the meta-atom array to apply a specific spatial phase gradient. The metasurface does not alter the underlying information carried by the signal; it solely dictates the wave propagation characteristics (beam direction, magnitude, and phase shift).

The channel coefficient $h_{p,r}$, which connects the metasurface operating with pattern p to receiver r, is defined by combining the complex array response in the receiver direction with the free-space path loss:

$$h_{p,r} = \frac{\mathrm{AF}_p(\theta_{rx,r})}{r_r}, \tag{9}$$

where $\mathrm{AF}_p(\theta_{rx,r})$ is the complex value of the array factor for the p-th pattern evaluated at the specific angle of the r-th receiver, carrying both magnitude and phase information.

Quadrature Phase Shift Keying (QPSK) modulation was selected for evaluation due to its robust noise immunity and widespread use in standard communication protocols. Each QPSK symbol consists of two orthogonal components [39], which are the in-phase (I) and quadrature (Q) components:

$$s_k = \frac{1}{\sqrt{2}}(b_I + jb_Q), \quad b_I, b_Q \in \{-1, +1\}. \tag{10}$$

The normalization factor $\frac{1}{\sqrt{2}}$ ensures a unitary symbol power ($|s_k|^2 = 1$). The received signal at receiver r under pattern p is modeled as:

$$y_{p,r} = h_{p,r}^{\mathrm{norm}} \cdot s_k + n, \tag{11}$$

where n represents the Additive White Gaussian Noise (AWGN), modeled as a complex number with real and imaginary components that are normally distributed with zero mean and variance $N_0/2$. N_0 is determined by the evaluated Signal-to-Noise Ratio (SNR):

$$N_0 = \frac{P_s}{\mathrm{SNR}_{\mathrm{lin}}}, \quad \mathrm{SNR}_{\mathrm{lin}} = 10^{\mathrm{SNR}_{\mathrm{dB}}/10} \tag{12}$$

where $P_s = 1$ is the normalized symbol power. The AWGN model effectively represents the accumulation of various environmental and thermal noise sources in the wireless link.

Monte Carlo simulations were performed in MATLAB using parameters detailed in Table 6.

TABLE 6. Communication performance calculation parameters.

Parameter	Value
Operating Frequency	5.67 GHz
Number of QPSK Symbols	10,000
Transmitter SNR	10 dB
Metasurface Height (H)	10 m

4.3. Spatial Selectivity and BER Analysis

To analyze the metasurface's spatial selectivity, we evaluate data streams under both "matched" (pattern aligned with the receiver angle) and "mismatched" (pattern aimed at a different receiver) conditions. For the qualitative constellation analysis, we transmitted 10,000 QPSK symbols per receiver. The qualitative results of the QPSK simulation are presented as constellation diagrams in Figures 6(a), (b), and (c). Figure 6(a) displays the reception when the $+20°$ pattern is activated. Rx1, positioned exactly at the target angle, has a highly coherent diagram with symbol points tightly clustered into the four ideal QPSK quadrants. This confirms that Rx1 is situated within the high-gain main beam. Conversely, Rx2 ($+30°$) and Rx3 ($+40°$) display severely dispersed symbol points scattered across I and Q planes without cluster formation. This indicates spatial isolation, as they receive only heavily attenuated sidelobe radiation. This behavior is highly consistent across all configurations. In Figure 6(b), activating the $+30°$ pattern yields clear clusters solely for Rx2. In Figure 6(c), the $+40°$ pattern isolates the clean signal exclusively to Rx3. The phase-coding scheme effectively creates an exclusive spatial communication channel for the targeted receiver, demonstrating excellent multi-user interference rejection.

To provide quantitative validation, we analyzed the Bit Error Rate (BER) as a function of Signal-to-Noise Ratio (SNR) (Figure 7). To ensure statistical reliability near the 10^{-3} threshold, we calculated the Bit Error Rate (BER) at each SNR point across five independent Monte Carlo trials, yielding an effective sample size of 500,000 bits. Furthermore, a single global

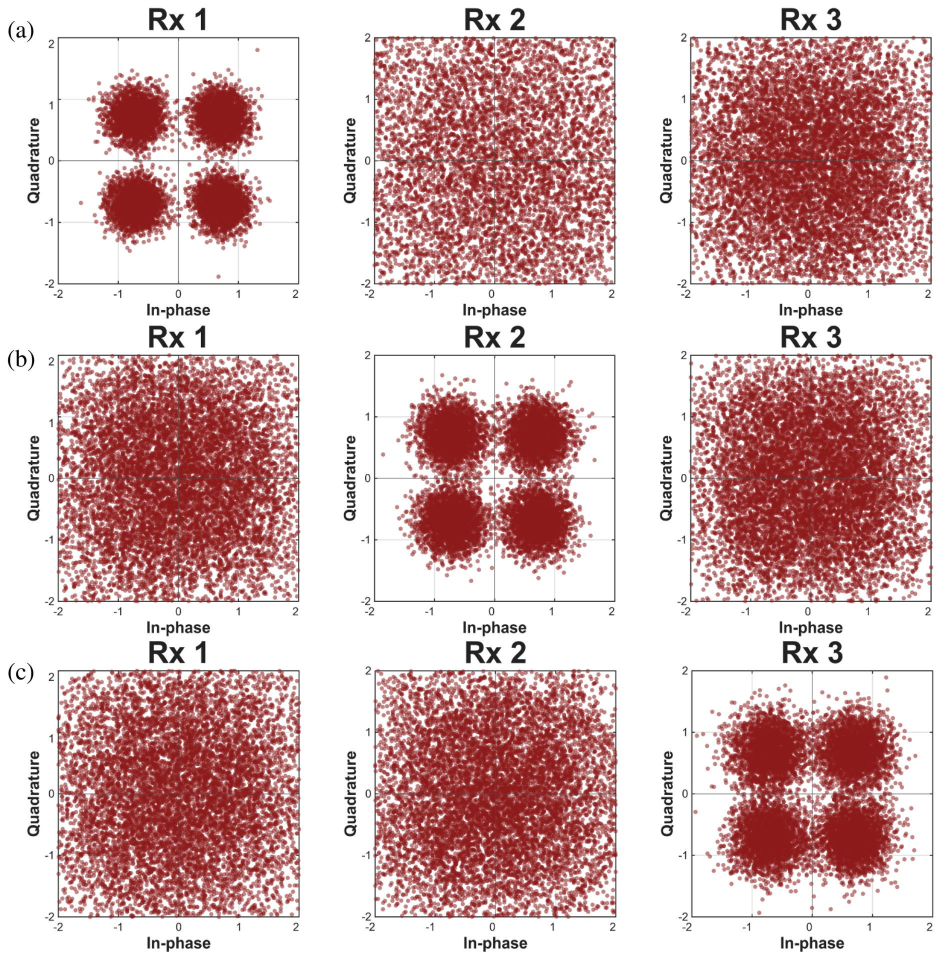

FIGURE 6. Received QPSK constellation diagrams illustrating multi-user interference rejection. Each panel shows the signal quality across three spatially distributed receivers when the metasurface beam is directed toward (a) $+20°$, (b) $+30°$, and (c) $+40°$.

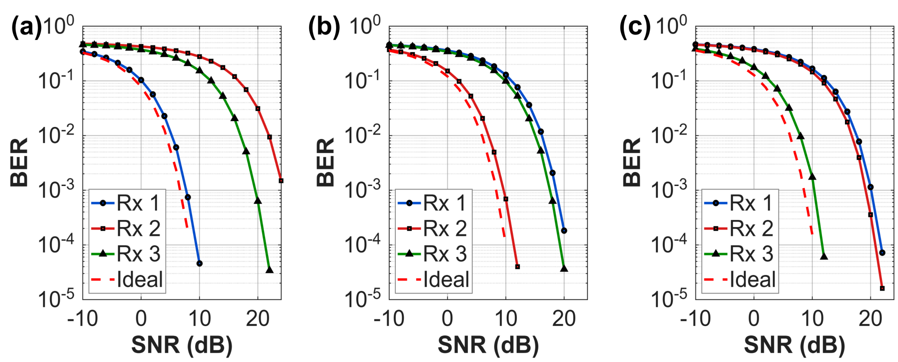

FIGURE 7. BER Curves as a function of SNR for target pattern configurations of: (a) $+20°$, (b) $+30°$, and (c) $+40°$.

channel normalization constant derived from the ideal 180° benchmark was applied uniformly in all configurations to guarantee that reported SNR advantages reflect true relative channel gains rather than normalization artifacts. As can be seen from Figure 7(a), when employing the $+20°$ pattern, the matched receiver (Rx1) demonstrates the steepest decline in BER, achieving a target BER of 10^{-3} at an SNR of merely 6 dB. In contrast, mismatched receivers (Rx2 and Rx3) require SNRs in excess of 20 dB to achieve equivalent reliability due to the low magnitude of sidelobe channels. Similar trends are observed across the scanning range. For the $+30°$ pattern, Rx2 reaches a 10^{-3} BER at 10 dB SNR, while the mismatched Rx1 and Rx3 curves nearly overlap, requiring 17 to 18 dB SNR (see Figure 7(b)). For the $+40°$ pattern, Rx3 reaches the 10^{-3} threshold at 10 dB SNR, outperforming the mismatched receivers by approximately 8 dB (Figure 7(c)). In conclusion, the system-level analysis proves that the proposed ultra-lightweight, row-column encoded metasurface provides a decisive SNR advantage for targeted receivers. To further quantify the impact of the non-ideal 143.15° phase contrast identified in Section 2.2, an ideal benchmark case (180° phase contrast, unity reflection amplitude) was additionally simulated under the same channel normalization reference and included in Figure 7 as a dashed reference curve. The results show that the matched receiver under the actual 143.15° phase-contrast configuration requires a modestly higher SNR than the ideal case to achieve the same BER target, quantifying the performance margin attributable to the non-ideal phase contrast and residual reflection loss of diode states relative to an ideal 1-bit reflectarray. By yielding an SNR gain of 8 to 14 dB compared to mismatched spatial configurations, the device establishes itself as a robust and highly deployable solution for maintaining reliable, spatially selective communication links in UAV-assisted NLoS environments.

It is important to note that within this analysis, the metasurface's array aperture gain is inherently embedded in the channel model, as the far-field array factor magnitude $|\mathrm{AF}_p(\theta_{rx,r})|$ directly represents the coherent combination of all 100 meta-atom contributions in the receiver direction, rather than treating the surface as a unity-gain reflector. Similarly, the surface's reflection efficiency is implicitly captured, since excitation amplitudes used in the Array Factor calculation ($a_{\mathrm{OFF}} = 0.858, a_{\mathrm{ON}} = 0.852$) correspond to the actual $|S_{11}|$ reflection magnitudes extracted from full-wave unit-cell simulation at 5.67 GHz, rather than assumed ideal (lossless) values. The receiver antenna gain is likewise implicitly accounted for within the evaluated SNR, consistent with standard link-budget conventions. We acknowledge, however, that the present model does not explicitly include polarization mismatch or channel fading/blockage effects. With a limitation considered in this study, this deliberate simplification isolates the spatial selectivity contributed strictly by the metasurface's phase encoding. Finally, omitted propagation effects would also influence the reported BER. Multipath fading introduces random amplitude and phase variations beyond the deterministic model in Equation (9). Furthermore, unintended UAV motion causes beam misalignment and Doppler shifts, potentially necessitating real-time beam tracking in a realistic scenario. These dynamic effects remain areas for future investigation.

5. CONCLUSION

Integrating Reconfigurable Metasurfaces (RMSs) with mobile aerial platforms offers a powerful solution for bypassing wireless network blockages; however, real-world deployment remains constrained by strict weight and payload limits. To address this issue, this paper presents the design and system-level analysis of a 1-bit reconfigurable metasurface operating at 5.67 GHz. By employing a row-column addressing architecture on a single-layer Rogers RO4003C substrate, the proposed design drastically reduced biasing network complexity — requiring only 20 control lines for a 10×10 array — minimizing the structural weight required for aerial integration. The array's electromagnetic performance was evaluated through a two-tier methodology. First, an analytical Array Factor (AF) model was utilized to synthesize optimal twin-beam phase configurations across a 120° field of view ($\pm 10^\circ$ to $\pm 60^\circ$). Subsequent full-wave validation in CST Microwave Studio confirmed that the metasurface achieves highly accurate adaptive beam steering for target angles up to $\pm 40^\circ$, maintaining beam direction deviations strictly below 1.5°.

To translate these physical-layer metrics into practical utility, we simulated the metasurface in a UAV-mounted communication scenario using Quadrature Phase Shift Keying (QPSK) modulation. To isolate the metasurface's spatial selectivity, the current evaluation uses a simplified channel model that omits complex propagation effects, such as multipath fading, blockage, and polarization mismatch. Within this controlled framework, the system demonstrated exceptional spatial selectivity. Qualitative constellation diagrams showed clean signal reception exclusively at targeted spatial coordinates, while quantitative Bit Error Rate (BER) analysis confirmed that targeted receivers gained an 8 to 14 dB Signal-to-Noise Ratio (SNR) advantage to achieve a 10^{-3} BER compared to mismatched channels. Despite these strong results within a $\pm 40^\circ$ scanning range, this study identified distinct limitations at extreme steering angles. For target angles of $\pm 50^\circ$ and $\pm 60^\circ$, significant discrepancies emerged between analytical AF predictions and physical full-wave simulations, resulting in severe beam-pointing errors and degraded side-lobe levels. This breakdown is attributed to the inherent limitations of the row-column architecture's phase quantization and the element-pattern roll-off at wide angles, which becomes increasingly dominant in highly complex, alternating ON/OFF phase-state distributions. Future studies will expand this operational range by integrating machine learning algorithms capable of predicting and compensating for mutual coupling effects during initial row-column pattern synthesis. Furthermore, subsequent phases of this research will focus on the physical fabrication of the metasurface prototype, empirical chamber measurements, and integrating propagation variables into a fully cascaded channel model that accounts for dynamic UAV flight conditions.

ACKNOWLEDGEMENT

This work was supported in part by the *Rumah Program* Internet of Things, Research Organization for Electronics and Informatics (OREI), National Research and Innovation Agency (BRIN), Indonesia, under Grant No. 18/III.6/HK/2026.

REFERENCES

[1] Andrews, J. G., S. Buzzi, W. Choi, S. V. Hanly, A. Lozano, A. C. K. Soong, and J. C. Zhang, "What will 5G be?" *IEEE Journal on Selected Areas in Communications*, Vol. 32, No. 6, 1065–1082, 2014.

[2] Miao, H., J. Zhang, P. Tang, L. Tian, X. Zhao, B. Guo, and G. Liu, "Sub-6 GHz to mmWave for 5G-advanced and beyond: Channel measurements, characteristics and impact on system performance," *IEEE Journal on Selected Areas in Communications*, Vol. 41, No. 6, 1945–1960, 2023.

[3] Rappaport, T. S., S. Sun, R. Mayzus, H. Zhao, Y. Azar, K. Wang, G. N. Wong, J. K. Schulz, M. Samimi, and F. Gutierrez, "Millimeter wave mobile communications for 5G cellular: It will work!" *IEEE Access*, Vol. 1, 335–349, 2013.

[4] Wu, Q. and R. Zhang, "Towards smart and reconfigurable environment: Intelligent reflecting surface aided wireless network," *IEEE Communications Magazine*, Vol. 58, No. 1, 106–112, 2020.

[5] Di Renzo, M., A. Zappone, M. Debbah, M.-S. Alouini, C. Yuen, J. D. Rosny, and S. Tretyakov, "Smart radio environments empowered by reconfigurable intelligent surfaces: How it works, state of research, and the road ahead," *IEEE Journal on Selected Areas in Communications*, Vol. 38, No. 11, 2450–2525, 2020.

[6] Basar, E., M. D. Renzo, J. D. Rosny, M. Debbah, M.-S. Alouini, and R. Zhang, "Wireless communications through reconfigurable intelligent surfaces," *IEEE Access*, Vol. 7, 116 753–116 773, 2019.

[7] Fathnan, A. A., K. Takimoto, M. Tanikawa, K. Nakamura, S. Sugiura, and H. Wakatsuchi, "Unsynchronized reconfigurable intelligent surfaces with pulse-width-based design," *IEEE Transactions on Vehicular Technology*, Vol. 72, No. 11, 15 103–15 108, 2023.

[8] Fathnan, A. A. and H. Wakatsuchi, "Controlling beam directions using self-reconfigurable time-varying metasurfaces," in *2023 XXXVth General Assembly and Scientific Symposium of the International Union of Radio Science (URSI GASS)*, 1–4, Sapporo, Japan, 2023.

[9] Cui, T. J., M. Q. Qi, X. Wan, J. Zhao, and Q. Cheng, "Coding metamaterials, digital metamaterials and programmable metamaterials," *Light: Science & Applications*, Vol. 3, No. 10, e218, 2014.

[10] Liaskos, C., S. Nie, A. Tsioliaridou, A. Pitsillides, S. Ioannidis, and I. Akyildiz, "A new wireless communication paradigm through software-controlled metasurfaces," *IEEE Communications Magazine*, Vol. 56, No. 9, 162–169, 2018.

[11] Takeshita, H., A. A. Fathnan, D. Nita, A. Nagata, S. Sugiura, and H. Wakatsuchi, "Frequency-hopping wave engineering with metasurfaces," *Nature Communications*, Vol. 15, No. 1, 196, 2024.

[12] Alhafid, A. K., S. Younis, and Y. E. Ali, "Enhanced far-field localization scheme using multi-RIS and efficient beam sweeping," *Progress In Electromagnetics Research C*, Vol. 140, 163–175, 2024.

[13] Zeng, Y., Q. Wu, and R. Zhang, "Accessing from the sky: A tutorial on UAV communications for 5G and beyond," *Proceedings of the IEEE*, Vol. 107, No. 12, 2327–2375, 2019.

[14] Xiao, Z., T. He, P. Xia, and X.-G. Xia, "Hierarchical codebook design for beamforming training in millimeter-wave communication," *IEEE Transactions on Wireless Communications*, Vol. 15, No. 5, 3380–3392, 2016.

[15] Lu, H., Y. Zeng, S. Jin, and R. Zhang, "Aerial intelligent reflecting surface: Joint placement and passive beamforming design with 3D beam flattening," *IEEE Transactions on Wireless Communications*, Vol. 20, No. 7, 4128–4143, 2021.

[16] Mozaffari, M., W. Saad, M. Bennis, Y.-H. Nam, and M. Debbah, "A tutorial on UAVs for wireless networks: Applications, challenges, and open problems," *IEEE Communications Surveys & Tutorials*, Vol. 21, No. 3, 2334–2360, 2019.

[17] Hum, S. V. and J. Perruisseau-Carrier, "Reconfigurable reflectarrays and array lenses for dynamic antenna beam control: A review," *IEEE Transactions on Antennas and Propagation*, Vol. 62, No. 1, 183–198, 2014.

[18] Yang, H., X. Cao, F. Yang, J. Gao, S. Xu, M. Li, X. Chen, Y. Zhao, Y. Zheng, and S. Li, "A programmable metasurface with dynamic polarization, scattering and focusing control," *Scientific Reports*, Vol. 6, No. 1, 35692, 2016.

[19] Pan, C., H. Ren, K. Wang, J. F. Kolb, M. Elkashlan, M. Chen, M. D. Renzo, Y. Hao, J. Wang, A. L. Swindlehurst, X. You, and L. Hanzo, "Reconfigurable intelligent surfaces for 6G systems: Principles, applications, and research directions," *IEEE Communications Magazine*, Vol. 59, No. 6, 14–20, 2021.

[20] Gong, S., X. Lu, D. T. Hoang, D. Niyato, L. Shu, D. I. Kim, and Y.-C. Liang, "Toward smart wireless communications via intelligent reflecting surfaces: A contemporary survey," *IEEE Communications Surveys & Tutorials*, Vol. 22, No. 4, 2283–2314, 2020.

[21] Yang, H., F. Yang, S. Xu, Y. Mao, M. Li, X. Cao, and J. Gao, "A 1-bit 10×10 reconfigurable reflectarray antenna: Design, optimization, and experiment," *IEEE Transactions on Antennas and Propagation*, Vol. 64, No. 6, 2246–2254, 2016.

[22] Wu, Q., S. Zhang, B. Zheng, C. You, and R. Zhang, "Intelligent reflecting surface-aided wireless communications: A tutorial," *IEEE Transactions on Communications*, Vol. 69, No. 5, 3313–3351, 2021.

[23] Zhang, L., X. Q. Chen, S. Liu, Q. Zhang, J. Zhao, J. Y. Dai, G. D. Bai, X. Wan, Q. Cheng, G. Castaldi, V. Galdi, and T. J. Cui, "Space-time-coding digital metasurfaces," *Nature Communications*, Vol. 9, No. 1, 4334, 2018.

[24] Kasda, D. A., A. A. Pramudita, and A. A. Fathnan, "Reconfigurable intelligent surface with 2 state reconfigurable element for wireless communication applications," in *2025 International Conference on Converging Technology in Electrical and Information Engineering (ICCTEIE)*, 124–128, Bandar Lampung, Indonesia, 2025.

[25] Khafagy, M., S. Fathi, and A. Magdy, "A low-complexity M-shaped reconfigurable intelligent meta-surface for mitigating pathloss in wireless systems," *Scientific Reports*, Vol. 15, No. 1, 24478, 2025.

[26] Barbuto, M., A. Alù, F. Bilotti, and A. Toscano, "Composite vortex manipulation as a design tool for reflective intelligent surfaces," *IEEE Antennas and Wireless Propagation Letters*, Vol. 22, No. 10, 2392–2396, 2023.

[27] Kamoda, H., T. Iwasaki, J. Tsumochi, T. Kuki, and O. Hashimoto, "60-GHz electronically reconfigurable large reflectarray using single-bit phase shifters," *IEEE Transactions on Antennas and Propagation*, Vol. 59, No. 7, 2524–2531, 2011.

[28] Zhang, J. W., Z. J. Qi, L. J. Wu, W. Cao, X. Gao, Z. H. Fu, J. Y. Chen, Z. X. Wang, S. R. Wang, J. W. Wu, Z. Zhang, J. N. Zhang, H. D. Li, J. Y. Dai, Q. Cheng, and T. J. Cui, "Multiple-partition cross-modulation programmable metasurface empowering wireless communications," *Laser & Photonics Reviews*, Vol. 19, No. 21, e00692, 2025.

[29] Dai, L., B. Wang, M. Wang, X. Yang, J. Tan, S. Bi, S. Xu, F. Yang, Z. Chen, M. D. Renzo, C.-B. Chae, and L. Hanzo, "Reconfigurable intelligent surface-based wireless communications: Antenna design, prototyping, and experimental results," *IEEE Access*, Vol. 8, 45 913–45 923, 2020.

[30] Nariyari, H. V., A. A. Fathnan, M. Z. Romdlony, B. A. Asy'ari, E. J. Pristianto, and H. S. Putra, "Design of a voltage control system for a microcontroller-based reconfigurable metasurface prototype," in *2025 9th International Conference on Instrumentation, Control, and Automation (ICA)*, 234–237, Bandung, Indonesia, 2025.

[31] Huang, C., B. Sun, W. Pan, J. Cui, X. Wu, and X. Luo, "Dynamical beam manipulation based on 2-bit digitally-controlled coding metasurface," *Scientific Reports*, Vol. 7, No. 1, 42302, 2017.

[32] Davoyan, A. and H. Atwater, "Perimeter-control architecture for optical phased arrays and metasurfaces," *Physical Review Applied*, Vol. 14, No. 2, 024038, 2020.

[33] Li, L., T. J. Cui, W. Ji, S. Liu, J. Ding, X. Wan, Y. B. Li, M. Jiang, C.-W. Qiu, and S. Zhang, "Electromagnetic reprogrammable coding-metasurface holograms," *Nature Communications*, Vol. 8, No. 1, 197, 2017.

[34] Tang, W., M. Z. Chen, X. Chen, J. Y. Dai, Y. Han, M. D. Renzo, Y. Zeng, S. Jin, Q. Cheng, and T. J. Cui, "Wireless communications with reconfigurable intelligent surface: Path loss modeling and experimental measurement," *IEEE Transactions on Wireless Communications*, Vol. 20, No. 1, 421–439, 2021.

[35] Huang, C., S. Hu, G. C. Alexandropoulos, A. Zappone, C. Yuen, R. Zhang, M. D. Renzo, and M. Debbah, "Holographic MIMO surfaces for 6G wireless networks: Opportunities, challenges, and trends," *IEEE Wireless Communications*, Vol. 27, No. 5, 118–125, 2020.

[36] Basar, E., "Reconfigurable intelligent surface-based index modulation: A new beyond MIMO paradigm for 6G," *IEEE Transactions on Communications*, Vol. 68, No. 5, 3187–3196, 2020.

[37] Balanis, C. A., *Antenna Theory: Analysis and Design*, John Wiley & Sons, 2016.

[38] Kraus, J. D., R. J. Marhefka, and A. S. Khan, *Antennas and Wave Propagation*, Tata McGraw-Hill Education, 2006.

[39] Sklar, B., *Digital Communications: Fundamentals and Applications*, Pearson, 2021.